Materials and Design 201 (2021) 109492

Contents lists available at ScienceDirect

Materials and Design

journal homepage: www.elsevier.com/locate/matdes

Printable smart 3D architectures of regenerated silk on poly (3-hydroxybutyrate-*co*-3-hydroxyvalerate)

Silvia Bittolo Bon [a,b,+], Irene Chiesa [c,+], Davide Morselli [b,d], Micaela Degli Esposti [b,d], Paola Fabbri [b,d], Carmelo De Maria [c], Tommaso Foggi Viligiardi [e], Antonino Morabito [e,f], Giacomo Giorgi [g,h], Luca Valentini [a,b,*]

[a] Dipartimento di Ingegneria Civile e Ambientale, Università degli Studi di Perugia, Strada di Pentima 4, 05100 Terni, Italy
[b] Italian Consortium for Science and Technology of Materials (INSTM), Via Giusti 9, 50121 Firenze, Italy
[c] Department of Ingegneria dell'Informazione and Research Center E. Piaggio, University of Pisa, Largo Lucio Lazzarino 1, 56122 Pisa, Italy
[d] Department of Civil Chemical, Environmental and Materials Engineering (DICAM), Università di Bologna, Via Terracini 28, Bologna 40131, Italy
[e] Department of Pediatric Surgery, Meyer Children's Hospital, Viale Pieraccini 24, 50139 Firenze, Italy
[f] Dipartimento Neuroscienze, Psicologia, Area del Farmaco e della Salute del Bambino NEUROFARBA, Università degli Studi di Firenze, Viale Pieraccini 6, 50121 Firenze, Italy
[g] Dipartimento di Ingegneria Civile e Ambientale (DICA), Università degli Studi di Perugia, Via G. Duranti 93, 06125 Perugia, Italy
[h] CNR-SCITEC, I-06123 Perugia, Italy

HIGHLIGHTS

- 3D printing of hybrid natural proteins and bio-based polymers
- Digitally designed 3D objects with self-powering properties
- Modeling the different thermal coefficient of expansion of the protein layer onto a biopolymer
- Engineering strategy to seal an anastomosis without the aid of mechanical sutures

GRAPHICAL ABSTRACT

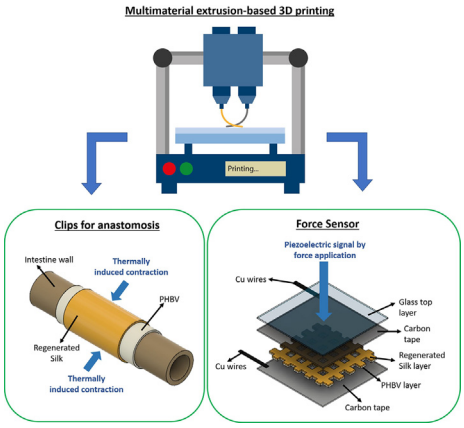

ARTICLE INFO

Article history:
Received 13 October 2020
Received in revised form 13 January 2021
Accepted 14 January 2021
Available online 18 January 2021

Keywords:
3D printing
Finite element analysis
Regenerated silk
PHBV
Sutureless device
Piezoelectric properties

ABSTRACT

In this study, we report the fabrication of two different three-dimensional (3D) architectures of regenerated silk (RS) and poly(3-hydroxybutyrate-*co*-3-hydroxyvalerate) (PHBV) with embedded functionalities. 3D printed cylinders with an internal layer of PHBV and an external of calcium ions (Ca^{++}) or potassium nitrate (KNO_3) modified RS were designed to control the radial shrinkage, water uptake and compression strength. Such cylinders were then used as sutureless thermoresponsive clips, measuring the bursting resistance once applied on an anastomized porcine intestine. Experimental data are supported by finite element simulations that model the tube contraction, demonstrating the possibility to program the shape-changing behavior of 3D printed structures. Printing RS on PHBV, we obtained responsive 3D grids to external force with self-powering properties. The synergic effect obtained by combining materials on appropriate architectures paves the way to potential clinical applications ranging from monitoring of vital signs to sutureless sealant patches.

* Corresponding author at: Dipartimento di Ingegneria Civile e Ambientale, Università degli Studi di Perugia, Strada di Pentima 4, 05100 Terni, Italy.
E-mail address: luca.valentini@unipg.it (L. Valentini).
+ co-first authorship

https://doi.org/10.1016/j.matdes.2021.109492

1. Introduction

Silk fibroin is an advanced biopolymer used for biomedical applications [1,2] that has thermoplastic properties [3]. Extracted from *Bombyx mori* (*B. mori*) cocoons, the dissolution methods of fibroin proteins regulate the regenerated silk (RS) assembly and thus the possibility to control its mechanical behavior, as reported in literature [4–10].

Silk polymorphism has been used to generate 3D bulk materials [11] and to generate interfaces with other polymers to obtain composite materials with stimulus-responsive behavior [12]. Water, methanol and ultraviolet (UV) external stimuli have been used to create micropatterned surfaces [13] and water absorption from wet tissue substrate generates a compressive strain on hybrid RS films, used as a sealant in an surgical anastomosis [14].

Bio-based polymers, that can be considered very promising for biomedical applications, include polyhydroxyalkanoates (PHAs) [15,16]. In particular, Poly(3-hydroxybutyrate-*co*-3-hydroxyvalerate) (PHBV) has generated much interest in the PHA family due to its biocompatibility and mechanical properties. PHBV has demonstrated good processability and has been extensively used to fabricate complex three-dimensional (3D) geometries for applications in tissue regeneration and clinical implementation [17–19].

RS and PHBV as individual materials have been studied and employed as biomaterial inks for 3D printing [20,21]. Their assembly in multifunctional composites are usually obtained with multi-step procedures (i.e. spin coating, nano lithography, dip coating etc) which are not selective and difficult to apply to complex geometries [13].

The use of additive manufacturing technologies, commonly referred as 3D printing, is extremely useful. 3D printing allows to control the spatial heterogeneity of chemical and physical properties of a 3D structure, through the precise and predetermined deposition of multiple materials during the same printing run, starting from a digital model [22,23].

3D printing permits both above mentioned materials to be placed in a specific and designed manner to fabricate complex architectures and to study the synergy of their properties, an issue that has not been yet investigated.

RS and PHBV are piezoelectric materials with potential clinical applications in the field of continuous monitoring of vital signs in hospital setting [24]. RS is also a sealant thermo-responsive material. In this study, we hypothesized their matching within multilayer 3D geometries, thus developing two multi-material devices of clinical interest. A 3D printed bilayer hollow tubular structure to be used as a sutureless clip for intestine anastomosis was developed. Anastomosis is the accurate union of two viable structures avoiding tension [25]. Sutureless anastomosis are deemed to be safe and can be achieved in various ways [26–28].

The strategy for the activation of our innovative 3D printed system, relies on the different thermal coefficients of expansion of the RS layer printed over the PHBV substrate. Thus, the ability of RS to contract over a tissue once the system is implanted into the human body is combined with the stability of PHBV to seal an anastomosis without the aid of mechanical sutures. Additionally the piezoelectric effect, that we previously observed on thermally coupled PHBV and RS bulk materials [12] was increased, by fabricating bilayer grids through extrusion-based 3D printing.

2. Experimental and methods

2.1. Materials

Sodium hydrogen carbonate ($NaHCO_3$), calcium chloride ($CaCl_2$), potassium nitrate (KNO_3), formic acid (FA), chloroform ($CHCl_3$) and poly(3-hydroxybutyrate-*co*-3-hydroxyvalerate) (PHBV, M_n 232,100 g mol^{-1}, M_w 684,700 g mol^{-1}, 23 mol% 3 HV units, custom grade) were supplied by Sigma-Aldrich. Prior to 3D fabrication, PHBV was purified according to the procedure described [29] in order to remove either production impurities or additives. The characterization of the purified polymer by proton nuclear magnetic resonance (^1H NMR) and gel permeation chromatography (GPC) has been previously reported in reference [12]. Purified PHBV was then dissolved in chloroform at different concentrations (50, 100 and 150 mg ml^{-1}) to obtain inks to use in the fabrication step.

B. mori cocoons were degummed in $NaHCO_3$ solution at 100 °C for 30 min to remove the sericin and isolate the fibroin component. Then, at 100 °C for 30 min; silk fibers were rinsed in deionized water to remove residual $NaHCO_3$. The complete treatment was repeated to assure the complete removal of sericin. Wet fibers were left to completely dry in air at room temperature.

The dry degummed silk fibers were dissolved in $CaCl_2$/FA solution (0.65 g of silk fibers in 5 ml of FA) to produce a silk solution with silk/$CaCl_2$ weight ratio 80:20 according to the following procedure. The calculated $CaCl_2$ amount was previously dissolved in 5 ml of FA using magnetic stirring, then the degummed silk fibers were added to the solution and stirred at room temperature for 5 min to obtain their complete solubilization. The samples obtained with this solution are identified in this work as RS + $CaCl_2$.

To prepare the silk/$CaCl_2$/KNO_3 solution, KNO_3 was added to the silk +$CaCl_2$ solution after silk fiber dissolution and it was stirred for 5 min at room temperature in an uncovered beaker. The KNO_3 amount was calculated as 3.5 wt% of the total weight of the solution. The samples obtained with this solution are identified in the present work as RS + KNO_3.

2.2. 3D printing of bilayer cylindrical structures

Hollow bilayer cylindrical structures (Fig. 1(a)) were 3D printed using a piston-driven extrusion-based 3D printer (Fig. 1(b)), featuring a rotating spindle (spindle diameter = 5 mm, spindle speed = 15 rpm, needle diameter = 0.8 mm) (inset of Fig. 1(b)). The inner layer was obtained extruding a 150 mg ml^{-1} PHBV solution in chloroform over the rotating spindle, whereas the external layer was made of silk compound using the same strategy. Two silk compounds were used (i.e. RS + $CaCl_2$ and RS + KNO_3). A tubular monolayer structure made of PHBV was fabricated as control. The cylinders were first created, then measured in diameter, and finally placed vertically on a petri dish and then placed in a desiccator (RH ≈ 60%, T ≈ 22 °C). To monitor the variation of the cylinder diameters without creating a significant distortion of the measurements, we acquired digital photos before and after conditioning and uploaded them into AUTOCAD 2012 software. Each image was scaled, taking as reference a graduated ruler and then four measurements of the diameter were made.

2.3. Materials characterization

The weight variation due to the water absorption of PHBV, RS + $CaCl_2$/PHBV and RS + KNO_3/PHBV tubes was monitored during the six days of exposure at 37 °C and 90% RH in climatic chamber (ACS DM1000C15ESS). Weight was recorded daily on three samples for each composition.

Fourier transform infrared (FTIR, Jasco FT/IR 615) analysis was performed in ATR mode from 1750 to 1450 cm^{-1} (amide I band). The analysis was repeated before and after sample conditioning in the climatic chamber (six days at 37 °C and 90% RH) to evaluate the changes in β-sheet fraction induced by the treatment. The spectra were deconvoluted by first smoothing the signal with a polynomial function with a 15-point

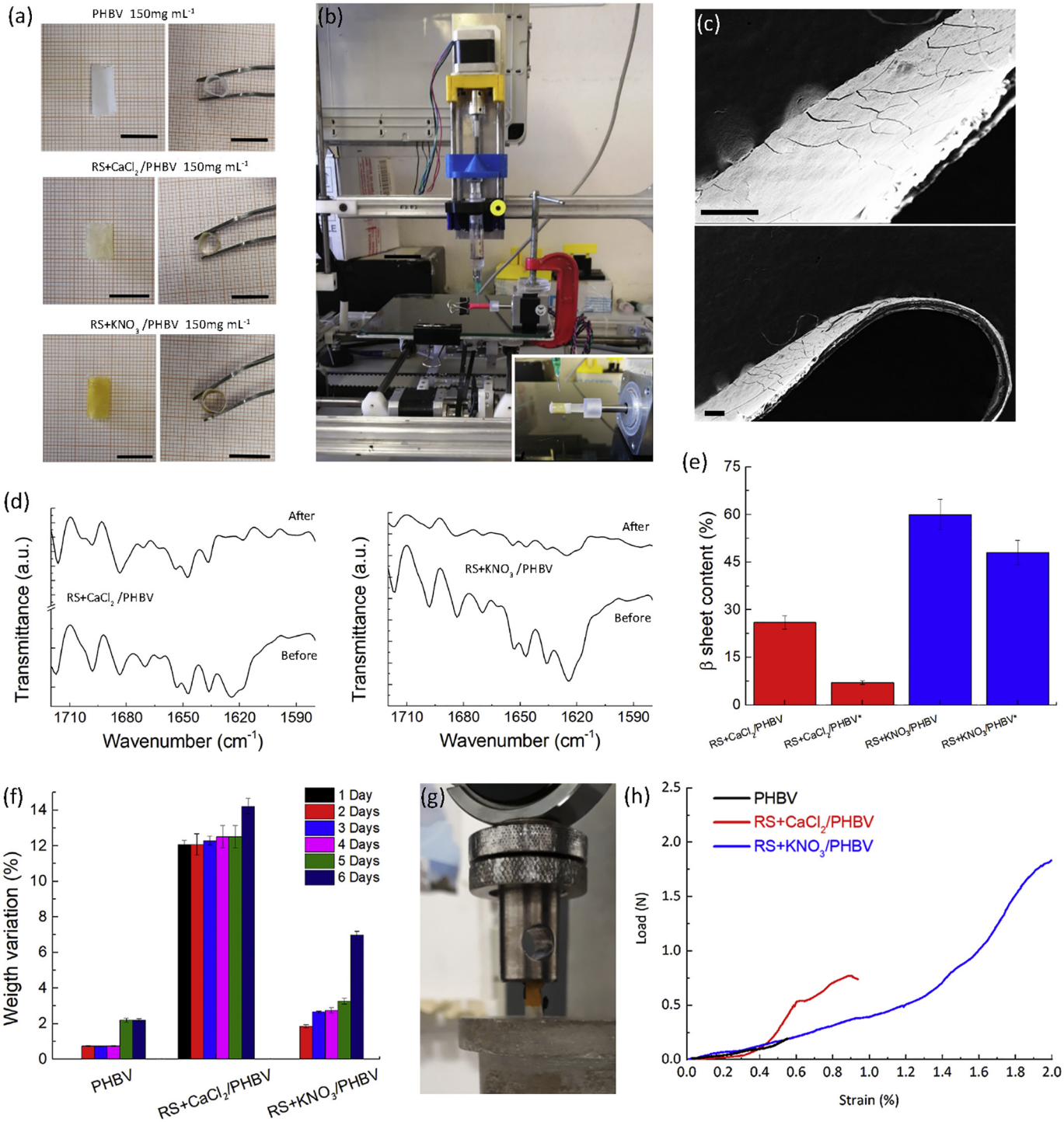

Fig. 1. (a) Top- and side-view of the fabricated PHBV (monolayer), RS + $CaCl_2$/PHBV and RS + KNO_3/PHBV cylindrical structures. Scale bar indicates 1 cm. (b) 3D printing equipment based on an extrusion system featuring a rotating spindle (highlighted in the inset) that was used for the fabrication of bilayer hollow cylindrical structures. (c) FESEM images demonstrating laminar structure and sidewall of RS/PHBV bilayer tube. Scale bars indicate 200 μm. (d) FTIR spectra of amide I wavenumber range (1580–1720 cm^{-1}) before and after the treatment in a climatic chamber for 6 days at 37 °C and 90% RH. (e) β-sheet fraction before and (*) after conditioning in the climatic chamber of RS + $CaCl_2$/PHBV (red colons) and RS + KNO_3/PHBV (blue colons) tubes, respectively. (f) Measurements of weight variation due to the water uptake of the fabricated cylindrical samples, during 6 days at 37 °C and 90% RH in the climatic chamber. (g) Compression tests equipment and used geometry. (h) Collapse force of PHBV, RS + $CaCl_2$/PHBV and RS + KNO_3/PHBV tubes.

Savitski—Golay smoothing function, subtracting a linear baseline and applying a Gaussian deconvolution of the curves by Origin 9 software.

Compressive mechanical properties were determined at a rate of 1 mm min^{-1} with a tensile testing machine (Lloyd Instr. LR30K) equipped with a 50 N static load cell. A minimum of three load curves were recorded for each sample.

The surface morphology was investigated by field emission scanning electron microscopy (FESEM, Zeiss Supra 25).

2.4. Finite element analysis of bilayer cylindrical structure activation

Finite element (FE) models were implemented in Comsol Multiphysics (Comsol Inc., 5.3) to analyze the contractile capability of the 3D printed cylindrical structures, due to the negative thermal expansion coefficient of the RS [30]. In all simulations, the Solid Mechanics application mode in stationary condition was used. 2D plane-strain models were designed with an out-of-plane thickness of 0.01 m. A total of 5 different models were implemented, with increased complexity and completeness: i) PHBV; ii) RS; iii) PHBV and RS; iv) PHBV + intestine wall; v) PHBV, RS and intestine wall (i.e. complete model) (Fig. S1). When RS was included, both RS compounds were simulated. In all subdomains, a linear elastic material model was used, with the addition of the thermal expansion model for the PHBV and RS; thermal expansion of the intestine wall was neglected. The strain reference temperature was set as 20 °C, whereas the working temperature was set at 37 °C (i.e. physiological temperature). Subdomain parameters are reported in Table S1. Boundary conditions of the complete model are reported in Fig. S1. Boundary conditions of the others model are not reported but can be easily deduced. The internal pressure of the intestine was introduced as boundary condition, equal to 2 kPa [36]. A triangular mesh, controlled by the physics, was used in all the simulations. Mesh statistics are shown in Table S2. For all the implemented models, the displacement in the point A and B (Fig. S1) was evaluated, and, in addition, in the models that included the intestine wall, the stress tensor along the r component in the point A and B was also analyzed.

2.5. Sutureless clip characterization

A customized system consisting of a peristaltic pump was used, together with a digital manometer, to measure and record the bursting pressure of the anastomosis, both the reference one without presence of the tube and the anastomosis treated with PHBV or RS/PHBV tubes. The bursting pressure is defined as the maximum pressure reached followed by a sharp loss in pressure. A porcine intestine was used to measure the bursting pressure; a polymeric coupler was placed inside the two portions of intestine and used to maintain them in contact in the correct position. For the experiment with PHBV/RS tubes, two tubes were positioned externally on the intestine portion. Zero pressure value was set when the water filled the entire line before the anastomosis; it was then inflated with water until the bursting. The intestine section was clamped at both ends and filled with water at a flow rate of 50 ml min^{-1}. Five tests were carried out. For comparison purpose, a porcine intestine loop was sectioned with a scalpel, the two loop cuts created were then anastomosed with 5/0 absorbable interrupted full thickness sutures using a synthetic absorbable monofilament made of the polyester (p-dioxanone).

2.6. 3D printing of bilayer grid structures

Bilayer grid structures were 3D printed on a glass microscope slide employing the piston-driven extrusion-based 3D printer used for cylindrical structures but equipped with two extruders and cylindrical needles. The gcode of the structure was generated by Slic3r® starting from a 1.5 cm cube and applying the following printing parameters: infill = 15%; print speed = 7.5 mm s^{-1}; flow = 1.1; needle diameter = 0.21 mm. The first layer of the structure was fabricated using the previously prepared PHBV-based ink, whereas the second one was obtained depositing silk fibroin ink. Three concentrations of PHBV and two silk compounds were used (six combinations). Monolayer grid structures made of PHBV were also fabricated as control. For each PHBV-silk combination, 10 images of the grid lines and pores were acquired with a brightfield microscope (Olympus AX70) and the width of the lines and pores was measured by ImageJ® (Table S3).

2.7. Piezoelectric force sensor assembling and testing

A piezoelectric device was fabricated as described in Scheme S1. The piezoelectric output of the bilayer grid device was measured applying an external force of 5 N at a frequency of 0.05 Hz. The open circuit voltage values were monitored using a computer controlled Keithley 4200 Source Measure Unit. The force was calculated with the finger imparting method [31]: when an object falls, first it touches the surface, and secondly, completely acts on the film surface. The object increases its velocity to a maximum value and then it decreases the velocity to zero. Thus, the force is calculated by using the momentum and kinetic energy theorem, as it follows:

$$m*g*h = (1/2)m*v^2 \quad (1)$$

$$(F - m*g)/Dt = m*v \quad (2)$$

where in (1,2) m is the mass of the falling object (expressed in [kg]), h is the falling height [m], v is the maximum falling velocity [m/s], F is the contact force [N], and Dt is the time variation [s] between the two consecutive voltage peaks. The average falling height (h) is ≈ 0.16 m and g = 9.80 N/kg. The applied force was calculated based on the above equations and mass data.

3. Results and discussions

3.1. Sutureless clips

The tubes, shown in Fig. 1(a), were fabricated by the extrusion-based 3D printer presented in Fig. 1(b) equipped with a rotating spindle (inset of Fig. 1(b)). Tubes are composed of two parts: the inner part, which is a cylindrical PHBV tube (5 mm diameter) and an outer part that is a tubular layer made of RS and fabricated by the same technique with a thickness of approx. 50 μm, as revealed by the morphological analysis of the tubes (Fig. 1(c)).

The laminar structure of the tube as well as the outer diameter and the sidewall thickness were confirmed by FESEM images reported in Fig. 1(c).

Silk fibroin is a protein based material that undergoes a sol–gel transition induced by the presence of salts [32,33]. The addition of $CaCl_2$ into a silk fibroin solution in FA leads to a β-sheet content of 20% that further reduces approximately to 7% after water absorption due to a treatment at 90% RH and 37 °C for six days. On the contrary, the addition of KNO_3 promotes the formation of the β-sheet intermolecular structures (Figs. 1(d) and 1(e)) and stable structures after aging in the same conditions. This result is in accordance with the observation of liquid-gel transition in silk fibroin that is generally promoted by salts, such as KNO_3, that behaves as cross-linking agent, i.e. the presence of a more cross-linked structure hinders permeation of water molecules (Fig. 1(f)) [34]. However, it is well known that the addition of $CaCl_2$ induces a chelation of the silk protein [35], leading to the adsorption of the water molecules from the environment; hence, the calcium ions (Ca^{++}) act as plasticizers, resulting in a lower content of β-sheets.

The radial strength of the cylinder was then investigated by compression tests (see Fig. 1(g)) in order to verify the maintaining radial tension during insertion of a vessel or portion of intestine. The collapse resistance of the PHBV and RS/PHBV was dependent on RS composition as shown in Fig. 1(h). The maximum load of 2 N was achieved by the RS + KNO_3/PHBV tubes, which is more than double the load found for the RS + CaCl2/PHBV tubes. This increase in the collapsing resistance agrees with the β-sheet content calculated from the prepared samples and an increase of the β-sheet content results in an enhancement of the tube's resistance to collapse.

Manual suturing is the current gold standard for closure of intestinal anastomoses. Reconstitution of intestinal portions with anastomosis remains a technically challenging and time-consuming procedure, which

requires a learning path challenging for surgeons. Suturing errors can lead to anastomotic leaks, prolonged hospital stays and in some cases even death. The first step is the evaluation of the tightness of the 3D printed tubes in a highly realistic situation. To this aim, the tube was inserted over a portion of an animal-origin intestine and was forced to resist the pressures that characterize the peristaltic movements of this organ in vivo.

Fig. 2(a), (b) and (c) illustrate how the cylinders for sutureless anastomosis were assembled; first two cylinders were inserted over the porcine intestine followed by inserting the coupler into the intestine. Finally, the device was put in a climatic chamber at 37 °C for 24 h in order to induce the shrinkage of the tubes and thus to obtain the desired sealing effect. For this proof of concept, we used RS + KNO_3/PHBV tubes, which have shown to be the most stable system. The resistance of the anastomotic seal was evaluated by measuring the bursting pressure (Fig. 2(d)). Intestinal anastomosis with mechanical sutures withstands low pressure before bursting (i.e. 37 mmHg) in accordance with our previous observations [14]. The use of the device presented here significantly improves the burst pressure. In particular, the use of the RS + KNO_3/PHBV tube increases the burst pressure to approximately 90 mmHg, an increment of over 140% in comparison to the value recorded for sutured intestine. This may be in part to the experimental observation that when the RS is included on the tubes they contract radially (negative displacement along radius), compressing the intestine. The compression is more pronounced when the RS + KNO_3 compound was used (Fig. 2(e) and Fig. S2).

Experimental data is supported by FE simulations that offer deeper insight into the mechanisms that lead to the observed shrinkage (Fig. 3(a), (b), (c) and Fig. S1). In detail, five different FE models were implemented, with increased complexity and completeness: i) PHBV; ii) RS; iii) PHBV and RS; iv) PHBV + intestine wall; v) PHBV, RS and intestine wall (complete model) to analyze the contractive behavior of the cylindrical structures. The displacement and stress tensors at the interfaces between the tube layers and the intestinal wall (point A and B in Fig. S1) showed that when the RS is included, the tubes contract radially at 37 °C, compressing the intestine wall with a stress tensor of the order of magnitude of kPa (Fig. 3(a) and (c)). The most pronounced compression is observed when the RS + KNO_3 compound is implemented, involving a radial displacement of the intestine wall–PHBV interface (point A) of 10 μm (Fig. 3(b)). FE analysis also highlighted that both material properties (e.g. elastic modulus) as well as structure properties (e.g. layer thickness) are the key parameters that can induce a radial contraction. For RS + KNO_3/PHBV and RS + $CaCl_2$/PHBV tubes the thermal expansion coefficient and layer thickness can be assumed the same, however RS + KNO_3/PHBV has a significantly higher elastic modulus (values summarized in Table S1), which mainly affects the observed radial compression.

3.2. Piezoelectric 3D grids

Several studies have recently reported the potentialities of 3D printed scaffolds with controllable pore size [36] and substrate piezoelectricity [37] to promote cell attachment and differentiation. We 3D printed bilayer grid structures, where the PHBV solution was extruded first, followed by the silk compound. PHBV monolayer grid structures were fabricated as control.

Exploiting 3D printing allowed a precise deposition of material as well as easy fabrication of aligned bilayer structures with no sign of detachment. The absence of detachment is due to the FA contained in the RS ink. When RS is extruded on the PHBV grid, the FA superficially dissolves the PHBV, thus ensuring a strong adhesion between PHBV and RS layers without damaging the PHBV grid.

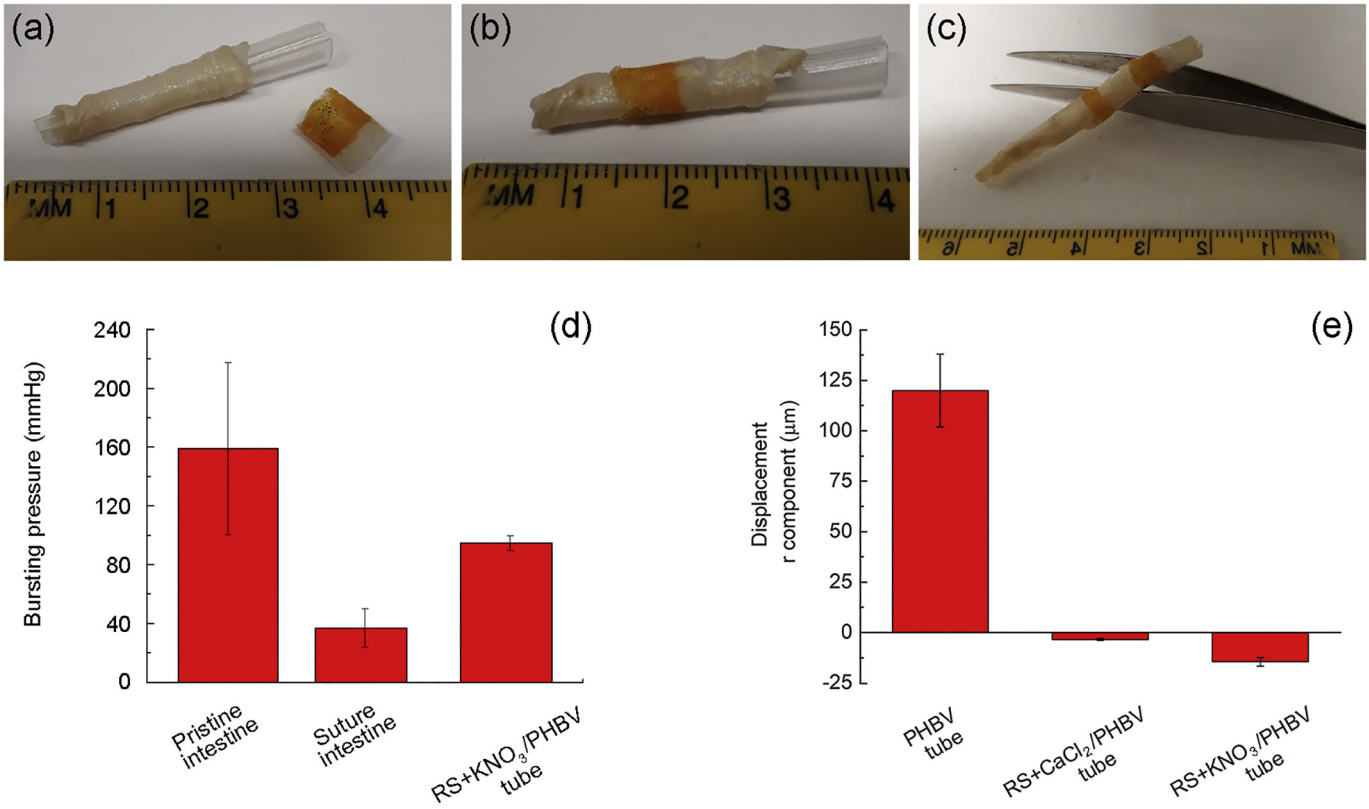

Fig. 2. Assembly of the fabricated device: (a) a silicone-based coupler was inserted into the porcine intestine; (b) the RS + KNO_3/PHBV tube was then inserted over the intestine and (c) finally a second RS + KNO_3/PHBV tube is used to seal the system. (d) Measured values of bursting pressure for the pristine intestine, sutured intestine and sutureless anastomosis RS + KNO_3/PHBV tube, respectively. (e) Measured values of the displacement of the cylinder radii of the prepared samples.

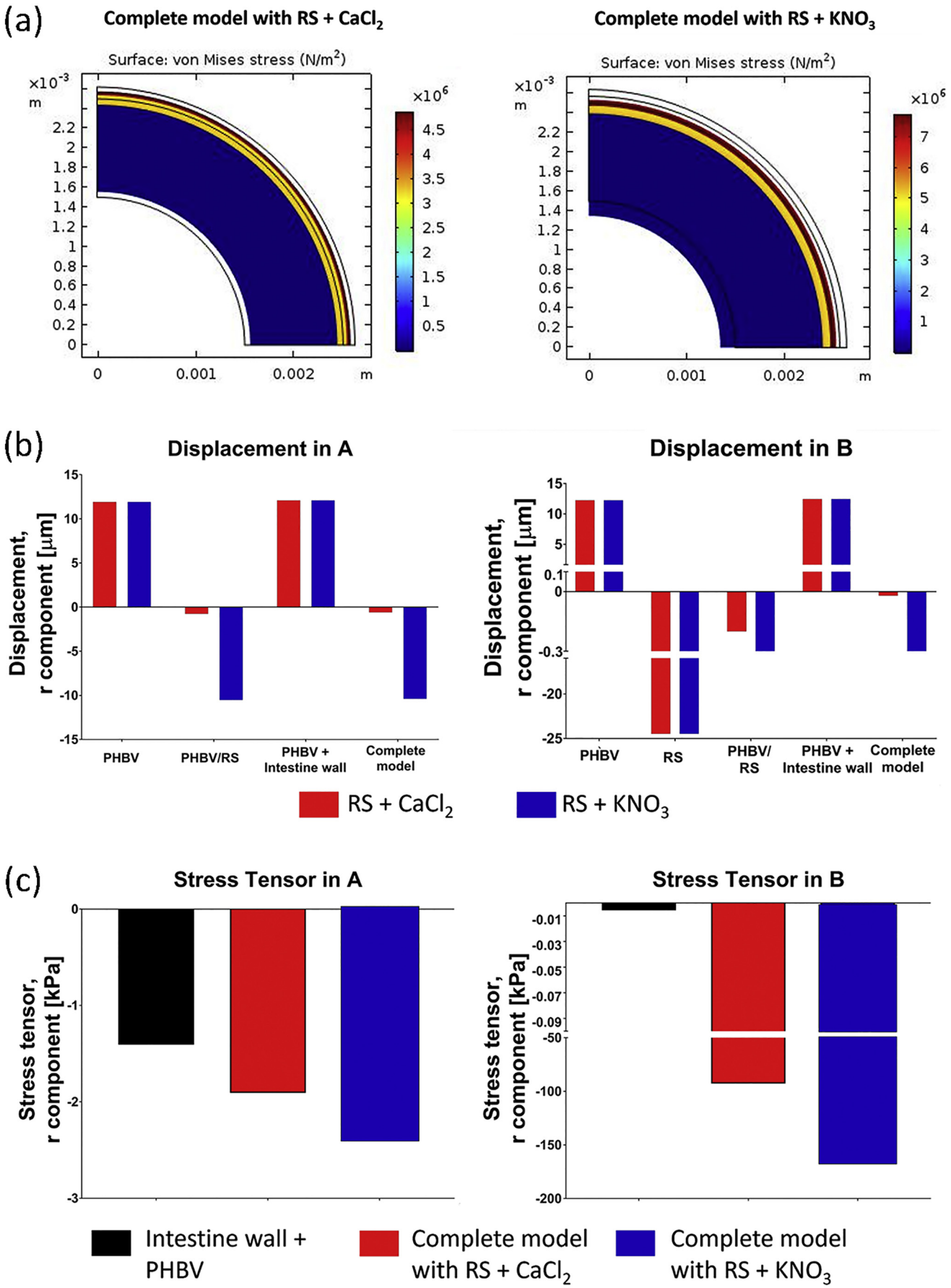
(a)
Complete model with RS + CaCl2
Surface: von Mises stress (N/m2)
×10-3 m
×10^6
Complete model with RS + KNO3
Surface: von Mises stress (N/m2)
×10-3 m
×10^6
(b)
Displacement in A
Displacement, r component [μm]
PHBV
PHBV/RS
PHBV + Intestine wall
Complete model
Displacement in B
Displacement, r component [μm]
PHBV
RS
PHBV/ RS
PHBV + Intestine wall
Complete model
RS + CaCl2
RS + KNO3
(c)
Stress Tensor in A
Stress tensor, r component [kPa]
Stress Tensor in B
Stress tensor, r component [kPa]
Intestine wall + PHBV
Complete model with RS + CaCl2
Complete model with RS + KNO3

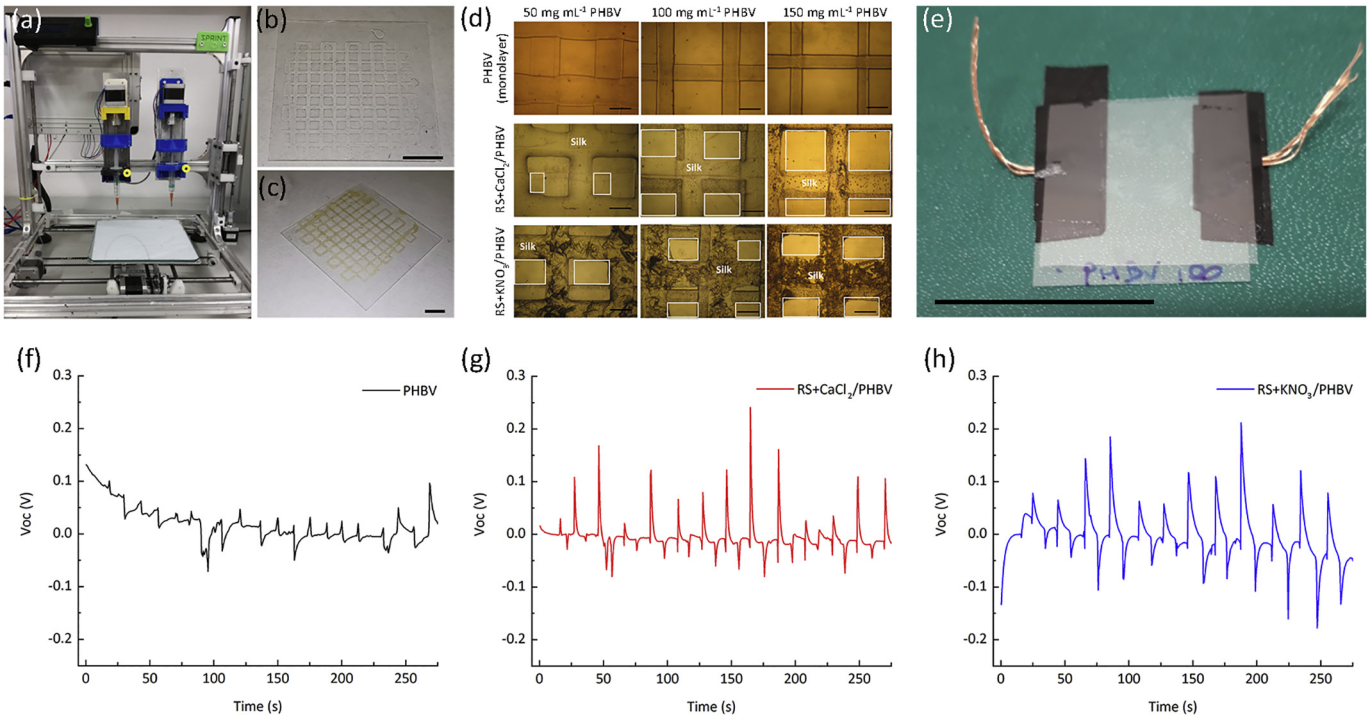

Fig. 4. (a) Piston-driven extrusion-based 3D printer used for the monolayer and bilayer grid fabrication. (b) Monolayer grid structures composed of PHBV. Scale bar indicates 5 mm. (c) Bilayer grid structures, composed of PHBV as lower layer and silk fibroin as upper layer. Scale bar indicates 5 mm. (d) Brightfield microscope images of the monolayer and bilayer 3D printed grid structures. Pores and silk grids are highlighted in white in the bilayer structures. Scale bars indicate 500 μm. (e) Photograph of the fabricated piezoelectric device (the scale bar indicates 2.5 cm). Generated open circuit voltage (V_{OC}) of (f) PHBV, (g) RS + $CaCl_2$/PHBV and (h) RS + KNO_3/PHBV piezoelectric devices as a function of the time.

This was also observed in the cylindrical 3D structures described in the previous section, where no detachment occurred between the two layers.

Images of the grid lines and pores were acquired by brightfield microscopy (Fig. 4(a), (b) and (c)) and their dimensions were evaluated using ImageJ®. Average dimensions and standard deviations of lines and pores shown in Fig. 4(d) are reported in Table S3 for monolayer and bilayer structures, respectively.

The line width is influenced by the nozzle size and rheology of the biomaterial ink [38]. It is noteworthy that by increasing the concentration of PHBV solution, the die swell of the material is extremely reduced, as the chloroform quickly evaporates before the ink spreads onto the deposition plane, leading to a significant increase in line resolution [39,40]. However, no significant differences can be observed in line and pore dimension when the different RS compounds are extruded. In addition, FA has a lower vapor pressure respect to chloroform, reducing the shape retention capability of the ink, leading to a final line width which triples the nozzle size.

After printing RS on PHBV we fabricated a piezoelectric force sensor by inserting the active bilayers grid (RS/PHBV) between two carbon tape electrodes and encapsulated the device with a top layer (Fig. 4 (e) and Scheme S1).

Fig. 4(f), (g) and (h) show open-circuit voltage signals of PHBV, RS-$CaCl_2$/PHBV and RS-KNO_3/PHBV grids respectively. The output voltages reported in Fig. 4(f), (g) and (h) were obtained by applying a constant load every 10 s and recording the signal. With consideration of the outputs generated from different RS/PHBV samples, the device with the RS + KNO_3 ink shows on average the largest difference between the maximum (press) and minimum (release) values. Furthermore, when we compare the difference between the press and release output signals of the samples reported in Fig. 4(g) and (h) with the respective RS β-sheet content reported in Fig. 1(e), in general there was an increase of the piezoelectric performance with an increase of the β-sheet content (i.e. the RS + KNO_3 based grid, Fig. 4(h)). These findings open a novel scenario for the employment of such materials for on-skin electronic monitoring of vital signs. These vital signs are important for monitoring of the patients' progress. Changing trends in patients' vital signs can indicate clinical deterioration, which, without identification and intervention, can lead to adverse consequences or death. In comparison to a recent study of Xu et al. [41] the output of our devices shows values that are similar to that obtained with Ag nanowires integrated on porous elastomer for electrocardiograms and electromyograms signals monitoring.

The origin of the piezoelectricity of the *B. mori* silk fibroin is related to the content of β-sheet crystallinity. In order to explain such effect we performed ab-initio computation of the Born Effective Charges (BECs) (details of calculation are reported in the Supporting Information section) of the model for the silk fibroin as suggested by Asakura et al. [42]. BECs (or dynamic effective charges) are quantities of paramount relevance that account for the coupling between lattice displacements and electrostatic field. BECs can be associated either to the change in polarization induced by the periodic displacement or to the force induced on each atom by an electric field. The optimized structure (Z = 4) reported in Fig. 5 (a) has the following lattice parameters, a = 9.19 Å b = 8.68 Å and c = 7.01 Å, in good agreement with previously reported data [42,43]. BEC variations between the isolated molecule (inset in Fig. 5(b)) and the bulk are reported in Table S4 along with the comparison of the nominal charge (calculated by means of a Bader

Fig. 3. Results from FE simulations. (a) Surfaces plot of complete models highlighting the contraction of the structure (Scale factor: complete model with RS + $CaCl_2$ = 100; complete model with RS + KNO_3 = 10). The model includes (b) the displacement along the r component and (c) the stress tensor along the r component in the point A and B (see Fig. S1).

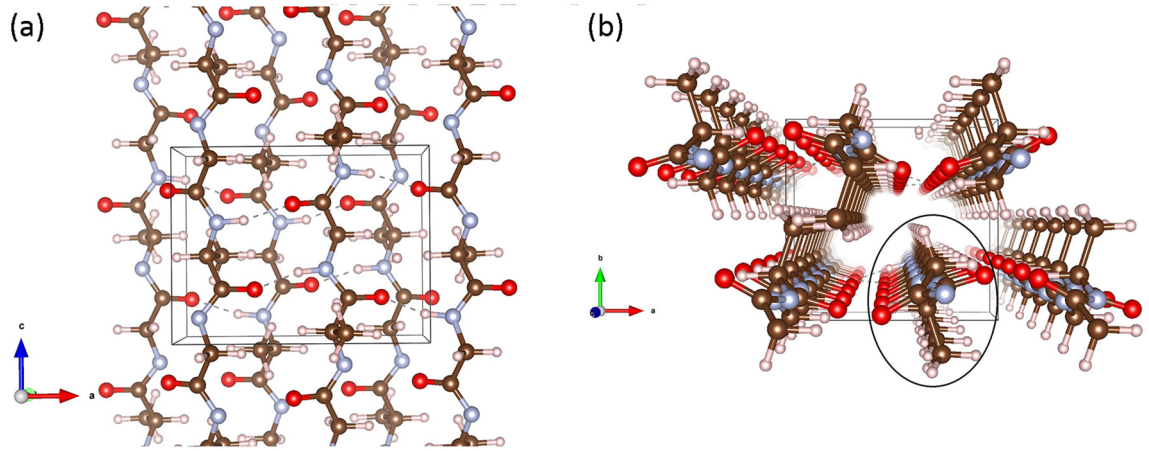

Fig. 5. (a) Lateral and (b) top view of the optimized structure of Silk Fibroin model [42]. The tetragonal solid line in (a) and (b) describes the unit cell. Inset in (b): isolated molecule (Red: O; Cyan: N; Brown: C; White: H atoms). (For interpretation of the references to colour in this figure legend, the reader is referred to the web version of this article).

charge partition, see Supporting Information for details) of atoms of interest. Differences from those obtained for the isolated molecule are clearly observable. The latter feature is expected, being ascribed to the presence of the crystalline structure, testifying that the van der Waals interactions dominate the dielectric features of this system.

4. Conclusions

In this study, we innovatively combined RS and PHBV by 3D printing two different smart architectures of biomedical interest. We have demonstrated the applications in 1) sutureless clip for intestine anastomosis and 2) a piezoelectric force sensor with self-powering properties. RS formulation with increased β-sheet content, was found to be stable in environmental conditions similar to those of the human body, thus opening novel scenarios for in vivo applications. Exploiting the advantaged of extrusion-based 3D printing, innovative and complex RS deposition patterns (i.e. honeycomb, helix) can be used to physically program the compressive properties of the sutureless clips. In contrast the infill density and pattern (e.g. honeycomb, gyroid, triangles, Hilbert curve) of the grid structure can be changed to improve the piezoelectric properties of the force sensor. In conclusion, this study has demonstrated the potential biomedical applications that arise from combining biomaterial smart properties and 3D printing technologies to rapid prototype bio-devices.

Declaration of Competing Interest

The authors declare that they have no known competing financial interests or personal relationships that could have appeared to influence the work reported in this paper.

Acknowledgments

S.B.B., I.C., D.M., M.D.E., P.F., and C.D.M., L.V., are supported by the Italian Ministry of Education, University and Research (MIUR) under the PRIN Project "Development and promotion of the Levulinic acid and Carboxylate platforms by the formulation of novel and advanced PHA-based biomaterials and their exploitation for 3D printed green-electronics applications" grant 2017FWC3WC.

Appendix A. Supplementary data

Supplementary data to this article can be found online at https://doi.org/10.1016/j.matdes.2021.109492.

References

[1] J.M. Lee, T. Chae, F.A. Sheikh, H.W. Ju, B.M. Moon, H.J. Park, Y.R. Park, C.H. Park, Three dimensional poly (ε-caprolactone) and silk fibroin nanocomposite fibrous matrix for artificial dermis, Mater. Sci. Eng. C 68 (2016) (2016) 758–767.
[2] O.J. Lee, J.-H. Kim, B.M. Moon, J.R. Chao, J. Yoon, H.W. Ju, J.M. Lee, H.J. Park, D.W. Kim, S.J. Kim, H.S. Park, C.H. Park, Fabrication and characterization of hydrocolloid dressing with silk fibroin nanoparticles for wound healing, Tissue Eng. Regen. Med. 13 (2016) 218–226.
[3] C. Guo, C. Li, H.V. Vu, P. Hanna, A. Lechtig, Y. Qiu, X. Mu, S. Ling, A. Nazarian, S.J. Lin, D.L. Kaplan, Thermoplastic Moulding of Regenerated Silk Nature Materials, 19, 2020 102–108.
[4] M.A. Brenckle, H. Tao, S. Kim, M. Paquette, D.L. Kaplan, F.G. Omenetto, Protein-protein nanoimprinting of silk fibroin films, Adv. Mater. 25 (2013) 2409–2414.
[5] A.N. Mitropoulos, G. Perotto, S. Kim, B. Marelli, D.L. Kaplan, F.G. Omenetto, Synthesis of silk fibroin micro- and submicron spheres using a co-flow capillary device, Adv. Mater. 26 (2014) 1105–1110.
[6] H. Tao, B. Marelli, M. Yang, B. An, M.S. Onses, J.A. Rogers, D.L. Kaplan, F.G. Omenetto, Inkjet printing of regenerated silk fibroin: from printable forms to printable functions, Adv. Mater. 27 (2015) 4273–4279.
[7] S. Kim, B. Marelli, M.A. Brenckle, A.N. Mitropoulos, E.-S. Gil, K. Tsioris, H. Tao, D.L. Kaplan, F.G. Omenetto, All-water-based electron-beam lithography using silk as a resist, Nat. Nanotechnol. 9 (2014) 306–310.
[8] S. Kim, A.N. Mitropoulos, J.D. Spitzberg, H. Tao, D.L. Kaplan, F.G. Omenetto, Silk inverse opals, Nat. Photonics 6 (2012) 817–822.
[9] F.G. Omenetto, D.L. Kaplan, New opportunities for an ancient material, Science 329 (2010) 528–531.
[10] H.J. Jin, D.L. Kaplan, Mechanism of silk processing in insects and spiders, Nature 424 (2003) 1057–1061.
[11] B. Marelli, N. Patel, T. Duggan, G. Perotto, E. Shirman, C. Li, D.L. Kaplan, F.G. Omenetto, Programming function into mechanical forms by directed assembly of silk bulk materials, Proc. Natl. Acad. Sci. U. S. A. 114 (2017) 451–456.
[12] S. Bittolo Bon, L. Valentini, M. Degli Esposti, D. Morselli, P. Fabbri, V. Palazzi, P. Mezzanotte, L. Roselli, Self-adhesive plasticised regenerated silk on poly(3-hydroxybutyrate-co-3-hydroxyvalerate) for bio-piezoelectric force sensor and microwave circuit design, J. Appl. Polym. Sci. 138 (2021) 49726.
[13] Y. Wanga, B.J. Kim, B. Peng, W. Li, Y. Wang, M. Li, F.G. Omenetto, Controlling silk fibroin conformation for dynamic, responsive, multifunctional, micropatterned surfaces, Proc. Natl. Acad. Sci. U. S. A. 116 (2019) 21361–21368.
[14] S. Bittolo Bon, M. Rapi, R. Coletta, A. Morabito, L. Valentini, Plasticised regenerated silk/gold nanorods hybrids as sealant and bio-piezoelectric materials, Nanomaterials 10 (2020) 179.
[15] Z. Li, J. Yang, X.J. Loh, Polyhydroxyalkanoates: opening doors for a sustainable future, NPG Asia Mater. 8 (2016), e265, .
[16] G.-Q. Chen, Q. Wu, The application of polyhydroxyalkanoates as tissue engineering materials, Biomaterials 26 (2005) 6565–6578.
[17] M. Zhou, D. Yu, Cartilage tissue engineering using PHBV and PHBV/bioglass scaffolds, Mol. Med. Rep. 10 (2014) 508–514.
[18] L. Brunetti, M. Degli Esposti, D. Morselli, A.R. Boccaccini, P. Fabbri, L. Liverani, Poly (hydroxyalkanoate)s Meet Benign Solvents for Electrospinning, 278, 2020 128389.
[19] X. Ye, L. Li, Z. Lin, W. Yang, M. Duan, L. Chen, Y. Xia, Z. Chen, Y. Lu, Y. Zhang, Integrating 3D-printed PHBV/calcium sulfate hemihydrate scaffold and chitosan hydrogel for enhanced osteogenic property, Carbohydr. Polym. 202 (2018) 106–114.
[20] R.R. Jose, W.K. Raja, A.M.S. Ibrahim, P.G.L. Koolen, K. Kim, A. Abdurrob, J.A. Kluge, S.J. Lin, G. Beamer, D.L. Kaplan, Rapid prototyped sutureless anastomosis device from self-curing silk bio-ink, J Biomed Mater Res B Appl Biomater 103 (2015) 1333–1343.
[21] A. Baradaran-Rafii, E. Biazar, S. Heidari-Keshel, Cellular response of limbal stem cells on PHBV/gelatin nanofibrous scaffold for ocular epithelial regeneration, Int. J. Polym. Mater. Polym. Biomater. 64 (2015) 879–887.

[22] C. De Maria, G. Vozzi, L. Moroni, Multimaterial, heterogeneous, and multicellular three-dimensional bioprinting, MRS Bull. 42 (2017) 578–584.
[23] M.A. Skylar-Scott, J. Mueller, C.W. Visser, J.A. Lewis, Voxelated soft matter via multimaterial multinozzle 3D printing, Nature 575 (2019) 330–335.
[24] M. Cardona-Morrell, M. Prgomet, R. Lake, M. Nicholson, R. Harrison, J. Long, J. Westbrook, J. Braithwaite, K. Hillman, Vital signs monitoring and nurse–patient interaction: a qualitative observational study of hospital practice, Int. J. Nurs. Stud. 56 (2016) 9–16.
[25] F. Goulder, Bowel anastomoses: the theory, the practice and the evidence base, World J. Gastrointest. Surg. 4 (2012) 208–213.
[26] J.L. McCue, R.K. Phillips, Sutureless intestinal anastomoses, Br. J. Surg. 78 (1991) 1291–1296.
[27] C. Fan, J. Ma, H. Zhang, Sutureless intestinal anastomosis with a novel device of magnetic compression anastomosis, R. Chin. Med. Sci. J. 26 (2011) 182–189.
[28] T.G. Hardy, W.G. Pace, J.W. Maney, A biofragmentable ring for sutureless bowel anastomosis, Dis. Colon Rectum 28 (1985) 484–490.
[29] M. Degli Esposti, F. Chiellini, F. Bondioli, D. Morselli, P. Fabbri, Highly porous PHB-based bioactive scaffolds for bone tissue engineering by in situ synthesis of hydroxyapatite, Mater. Sci. Eng. C 100 (2019) 286–296.
[30] N. Agarwal, D.A. Hoagland, R.J. Farris, Effect of moisture absorption on the thermal properties of *Bombyx mori* silk fibroin films, J. Appl. Polym. Sci. 63 (1997) 401–410.
[31] C. Hou, T. Huang, H. Wang, H. Yu, Q. Zhang, Y. Li, A strong and stretchable self-healing film with self-activated pressure sensitivity for potential artificial skin applications, Sci. Rep. 3 (2013) 3138.
[32] X. Wu, J. Hou, M. Li, J. Wang, D.L. Kaplan, S. Lu, Sodium dodecyl sulfate-induced rapid gelation of silk fibroin, Acta Biomater. 8 (2012) 2185–2192.
[33] A. Matsumoto, J. Chen, A.L. Collette, U.J. Kim, G.H. Altman, P. Cebe, D.L. Kaplan, Mechanisms of silk fibroin sol-gel transitions, J. Phys. Chem. B 110 (2006) 21630–21638.
[34] D.S. Im, M.H. Kim, Y. Il Yoon, W.H. Park, Gelation behaviors and mechanism of silk fibroin according to the addition of nitrate salts, Int. J. Mol. Sci. 17 (2016) 1697.
[35] A.K. Katz, J.P. Glusker, S.A. Beebe, C.W. Bock, Calcium ion coordination: a comparison with that of beryllium, magnesium, and zinc, J. Am. Chem. Soc. 118 (1996) 5752–5763.
[36] C. Xie, Q. Gao, P. Wang, L. Shao, H. Yuan, J. Fu, W. Chen, Y. He, Structure-induced cell growth by 3D printing of heterogeneous scaffolds with ultrafine fibers, Mater. Des. 181 (2019) 108092.
[37] A.K. Panda, R. K., A. Gebrekrstos, S. Bose, Y.S. Markandeya, B. Mehta, B. Basu, Tunable substrate functionalities direct stem cell fate toward electrophysiologically distinguishable neuron-like and glial-like cells, ACS Appl. Mater. Interfaces (2020) https://doi.org/10.1021/acsami.0c17257.
[38] N. Paxton, W. Smolan, T. Böck, F. Melchels, J. Groll, T. Jungst, Proposal to assess printability of bioinks for extrusion-based bioprinting and evaluation of rheological properties governing bioprintability, Biofabrication 9 (2017), 044107, .
[39] G. Vozzi, A. Previti, D. De Rossi, A. Ahluwalia, Microsyringe-based deposition of two-dimensional and three-dimensional polymer scaffolds with a well-defined geometry for application to tissue engineering, Tissue Eng. 8 (2002) 1089–1098.
[40] M. Mattioli-Belmonte, C. De Maria, C. Vitale-Brovarone, F. Baino, M. Dicarlo, G. Vozzi, Pressure-activated microsyringe (PAM) fabrication of bioactive glass–poly(lactic-co-glycolic acid) composite scaffolds for bone tissue regeneration, J. Tissue Eng. Regen. Med. 11 (2017) 1986–1997.
[41] Y. Xu, B. Sun, Y. Ling, Q. Fei, Z. Chen, X. Li, P. Guo, N. Jeon, S. Goswami, Y. Liao, S. Ding, Q. Yu, J. Lin, G. Huang, Z. Yan, Multiscale porous elastomer substrates for multifunctional on-skin electronics with passive-cooling capabilities, Proc. Natl. Acad. Sci. U. S. A. 117 (2020) 205–213.
[42] T. Asakura, T. Ohata, S. Kametani, K. Okushita, K. Yazawa, Y. Nishiyama, K. Nishimura, A. Aoki, F. Suzuki, H. Kaji, A.S. Ulrich, M.P. Williamson, Intermolecular packing in *B. mori* silk fibroin: multinuclear NMR study of the model peptide (ala-gly)15 defines a heterogeneous antiparallel antipolar mode of assembly in the silk II form, Macromolecules 48 (2015) 28–36.
[43] A. Roy, R. Prasad, S. Auluck, A. Garg, First-principles calculations of Born effective charges and spontaneous polarization of ferroelectric bismuth titanate, J. Phys.: Condens. Matter 22 (2010) 165902–165910.